Available online at www.sciencedirect.com

ScienceDirect

MATTER AND RADIATION AT EXTREMES

Matter and Radiation at Extremes 1 (2016) 249–256

www.journals.elsevier.com/matter-and-radiation-at-extremes

Research Article

Generation of a sharp density increase in radiation transport between high-Z and low-Z plasmas

Guangwei Meng [a], Jianguo Wang [a,*], Xuerong Wang [a], Jinghong Li [a,b], Weiyan Zhang [c,**]

[a] *Institute of Applied Physics and Computational Mathematics, Beijing 10094, China*
[b] *Laboratory of Computational Physics, Beijing 100088, China*
[c] *National Hi-Tech Inertial Confinement Fusion Committee of China, Beijing 100088, China*

Received 1 April 2016; revised 13 July 2016; accepted 10 August 2016
Available online 24 September 2016

Abstract

A sharp density increase (referred to as density incrustation) of the Au plasmas in the radiative cooling process of high-Z Au plasmas confined by low-Z CH plasmas is found through the radiative hydrodynamic simulations. The temperature of Au plasmas changes obviously in the cooling layer while the pressure remains constant. Consequently, the Au plasmas in the cooling layer are compressed, and the density incrustation is formed. It is also shown that when the high-Z plasma opacity decreases or the low-Z plasma opacity increases, the peak density of the density incrustation becomes lower and the thickness of the density incrustation becomes wider. This phenomenon is crucial to the Rayleigh–Taylor instability at the interface of high-Z and low-Z plasmas, since the density variation of Au plasmas has a considerable influence on the Atwood number of the interface.

PACS codes: 52.55.Dy; 52.25.Kn; 95.30.Jx

Keywords: Density incrustation; Radiation hydrodynamics; Opacity

1. Introduction

Radiative shocks are fundamental radiation hydrodynamic phenomena in astrophysics [1–4], which are of great importance in many astrophysical processes, including supernova explosions [5], supernova remnants [6–9], and accretion flows [10,11].

During the propagation of the radiative shocks, the radiation transport process has a significant influence on the states of upstream and downstream matters [12,13]. When the upstream matter passes through the shockwave front, it is compressed and heated to high temperature. Then the hot matter enters the cooling layer region. In this region, the hot materials release energy to the upstream materials through radiation transport. As the hot matter passes through the cooling layer, its temperature decreases while density increases before it reaches the final downstream state. The temperature distribution in the cooling layer forms a peak, and the maximum temperature appears at the shock front. Radiative shocks were firstly observed by Bozier in laboratory in 1986 [14]. After that, radiative shocks have been studied using Inertial Confinement Fusion (ICF) facilities around the world [15–23]. The state of the cooling layer was investigated by several experiments [20–22], and the density increase caused by radiative cooling is reported by these experiment results.

In our research on radiative shocks, we found that in the systems including both high-Z and low-Z plasmas [24], there was an incrustation of higher density near the interface of

* Corresponding author.
** Corresponding author.
E-mail addresses: wang_jianguo@iapcm.ac.cn (J.G. Wang), zw-y@vip.sina.com (W.Y. Zhang).

Peer review under responsibility of Science and Technology Information Center, China Academy of Engineering Physics.

http://dx.doi.org/10.1016/j.mre.2016.09.001

high-Z plasmas, which was different from the temperature peak in the cooling layer of radiative shocks, and the profile of the density incrustation was stable for a long time. This phenomenon is crucial to the Rayleigh–Taylor instability (RTI) at the interface of high-Z and low-Z plasmas. The density incrustation increases the Atwood number of the interface, thus it tends to accelerate the RTI growth at the interface. Moreover, the density incrustation can change the opacity of the high-Z plasmas near the interface. It is known that the radiation flux passing through the interface is determined mostly by the opacity of high-Z plasmas. Hence the density incrustation affects the radiation flux. In the gas filled hohlraum, a density increase was observed in the laser ablated Au plasma adjacent to the filling gas [25]. Simulation shows that its formation mechanism is similar to that of density incrustations [26].

In this paper, we studied the radiative cooling process of the hot high-Z Au plasmas which is confined by cold low-Z CH plasmas, and investigated the generation mechanism of the density incrustation. In Section 2, the theoretical methods are briefly outlined. In Section 3, the phenomenon of the density incrustation is introduced, and a detailed analysis of its formation mechanism is presented. In Section 4, the conclusion is given.

2. Theory

In this paper, three levels of theoretical methods are adopted to characterize the radiation transport process, which are the radiative heat conduction approximation, radiative diffusion approximation and radiative transfer equation. In the radiative heat conduction approximation, the motion of 1-D planar plasmas can be described by the following radiation hydrodynamic equations:

$$\frac{\mathrm{d}\rho}{\mathrm{d}t}+\rho\frac{\partial u}{\partial x}=0, \tag{1a}$$

$$\rho\frac{\mathrm{d}u}{\mathrm{d}t}+\frac{\partial p}{\partial x}=0, \tag{1b}$$

$$\rho c_{v\mathrm{e}}\frac{\mathrm{d}T_e}{\mathrm{d}t}+\rho T_{\mathrm{e}}\left(\frac{\partial p_{\mathrm{e}}}{\partial T_{\mathrm{e}}}\right)_{\rho}\frac{\mathrm{d}}{\mathrm{d}t}\left(\frac{1}{\rho}\right)+\frac{\partial F_{\mathrm{e}}}{\partial x}=-w_{\mathrm{er}}-w_{\mathrm{ei}}, \tag{1c}$$

$$\rho c_{v\mathrm{i}}\frac{\mathrm{d}T_{\mathrm{i}}}{\mathrm{d}t}+p_{\mathrm{i}}\frac{\mathrm{d}}{\mathrm{d}t}\left(\frac{1}{\rho}\right)+\frac{\partial F_{\mathrm{i}}}{\partial x}=w_{\mathrm{ei}}, \tag{1d}$$

$$\rho c_{v\mathrm{r}}\frac{\mathrm{d}T_{\mathrm{r}}}{\mathrm{d}t}+\frac{\partial F_{\mathrm{r}}}{\partial x}+p_{\mathrm{r}}\frac{\mathrm{d}}{\mathrm{d}t}\left(\frac{1}{\rho}\right)=w_{\mathrm{er}}, \tag{1e}$$

where Eqs. (1a) and (1b) are the mass and momentum conservation equations, and Eqs. (1c)–(1e) are the energy conservation equations of electron, ion and radiation. In Eq. (1), x and t represent space and time respectively; ρ and u are the density and velocity respectively; p_{r}, p_{e}, p_{i} are the pressure of radiation, electron and ion respectively, and $p=p_{\mathrm{r}}+p_{\mathrm{e}}+p_{\mathrm{i}}$ is the total pressure of plasmas; c_v, T and F are the constant-volume specific heat, temperature and flux, where the subscripts e, i and r of c_v represent the electron, ion and radiation; w_{er} and w_{ei} are the rate of radiation-electron energy exchange and the rate of ion-electron energy exchange.

Compared with the radiative heat conduction approximation, the radiative diffusion approximation is a relatively accurate description of radiation hydrodynamic process, in which Eq. (1e) should be modified as the following radiative diffusion equation

$$\frac{\partial E_\nu}{\partial t}-\mathrm{div}(D_\nu \mathrm{grad}E_\nu)=\sigma'_\nu[B_\nu(T_{\mathrm{e}})-E_\nu], \tag{2}$$

where ν is the photon energy, E_ν is the radiation energy density, D_ν is the radiation diffusion coefficient, σ'_ν is the effective absorption coefficient, $B_\nu(T_{\mathrm{e}})$ is the Planck function.

The radiative transfer equation is the most precise description on the radiation energy transport processes. The equation is expressed as

$$\frac{1}{c}\frac{\mathrm{d}I_\nu(\boldsymbol{\Omega})}{\mathrm{d}t}+\boldsymbol{\Omega}\cdot\nabla I_\nu(\boldsymbol{\Omega})=\sigma'_\nu\left[\frac{cB_\nu(T_{\mathrm{e}})}{4\pi}-I_\nu(\boldsymbol{\Omega})\right], \tag{3}$$

where I_ν is the radiation intensity, $\boldsymbol{\Omega}$ is the direction of photons. The radiative transfer equation is equivalent to the Boltzmann equation of the photons.

The system investigated is in 1-D planar geometry consisting of two materials: Au and CH. The thickness and density of Au are 1000 μm and 19.24 g/cm^3 respectively. The corresponding parameters for CH are 1000 μm and 10 g/cm^3. At the beginning, the Au plasma is heated to high temperature (1.0 keV in this model), while the CH plasmas are at low temperature (1.0 eV). Both boundaries of the model are free. Based on the radiative heat conduction approximation, the 20-group radiative diffusion approximation and the 20-group radiative transfer equations with S8 angular quadrature scheme, we simulated the radiation hydrodynamic process of the system using the Radiation Diffusion code in Multi Group (RDMG) code [27]. The angular resolution of radiative transfer simulations was carefully chosen to ensure that the results are convergent to the higher order S_N simulations. RDMG is a 1-D radiation hydrodynamic code, which can solve multi-group radiative transfer or diffusion equations in Lagrangian meshes under 1-D planar or 1-D sphere geometry. In this code, the electrons are assumed to be in thermal equilibrium with temperature T_{e}. The ions are in the same assumption with temperature T_{i}, where the electron temperature and the ion temperature can be different. In the simulation, the photon energy varied from 10^{-3} eV to 50 keV, and the tabulated opacity was used, which was calculated by OPacity code IN CHina (OPINCH) [28] based on a relativistic Hartree–Fock–Slater (HFS) self-consistent average atom model. The equation of state (EOS) of CH plasmas was that of fully-ionized gases, and the EOS data of Au plasmas came from our unpublished scientific report. If the temperature of Au plasma is 1 keV and the density is 19.24 g/cm^3, then the plasma pressure calculated by our EOS is 4.3 Gbar, and the pressure of fully-ionized Au plasma is 7.5 Gbar in this condition.

3. Simulation results and discussions

The radiation hydrodynamic motion of the system is displayed in Fig. 1. It is shown that there are shock waves, rarefaction waves and heat wave interacting with each other during the evolution of the system. At the initial stage, the pressure of the Au plasmas is much higher than that of the CH plasmas. So the Au plasmas compress the CH plasmas, push the Au/CH interface towards CH, and drive a shock wave in CH. The expansion of Au produces a rarefaction wave propagating from the Au/CH interface to the interior of Au plasmas.

Due to the high temperature, the Au plasmas release energy to CH plasmas, and drive a heat wave into CH. In this system, the heat wave is subsonic, which means that the velocity of the heat wave front is smaller than the local sound speed. At the early stage (before 0.2 ns) the heat wave front propagates together with the shock wave front. Then the heat wave slows down, the shock wave moves ahead of the heat wave, and the heat wave propagates in the downstream region of the shock wave in CH.

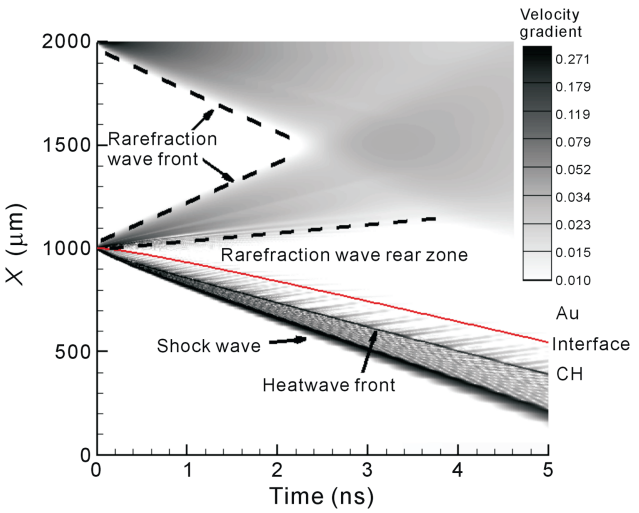

Fig. 1. The radiation hydrodynamic motion of the system. The gray scale represents the absolute value of velocity gradient in $(0.1\ \mathrm{ns})^{-1}$. This value indicates whether the plasma is in compression or expansion. The red line is the trajectory of CH-Au interface.

The density distributions obtained from the radiation heat conduction approximation at different time are shown in Fig. 2. The density incrustation arises near the interface when Au plasmas expand toward CH. The density of the Au plasmas reaches the peak value (referred to as the height of the density incrustation) at the Au/CH interface, while it decreases from the interface to the interior of Au plasmas. In Fig. 2(a), the density distributions from 0.002 ns to 0.05 ns are presented. During this period the boundary density of Au plasma rises quickly from 19.24 g/cm^3 to 32 g/cm^3, and the density incrustation grows up gradually. In Fig. 2(b) the density distributions at 1.0 ns, 3.0 ns and 5.0 ns are presented. From 1.0 ns to 5.0 ns, the height and the profile of the density incrustation are stable although the CH-Au interface moves rapidly. There are slight density fluctuations in the downstream region of the shock wave in CH plasmas as a result of the numerical error induced by the pseudo-viscosity method used in the simulation.

In order to verify the density incrustation, the radiation hydrodynamic evolution of this system was also simulated based on the 20-group radiative diffusion approximation and 20-group radiative transfer equations, as shown in Fig. 3. Similar density incrustations are observed in these radiation models, which indicates that the density incrustation is independent of the radiation models. Because the radiative transfer equation is the most accurate method, the results hereafter were obtained from the radiative transfer simulations.

It is known that the effect of wall heating [29,30] can also cause the density perturbation to be similar to the phenomenon of the density incrustation, but the spatial scale of the density perturbation caused by the wall heating effect is dependent on

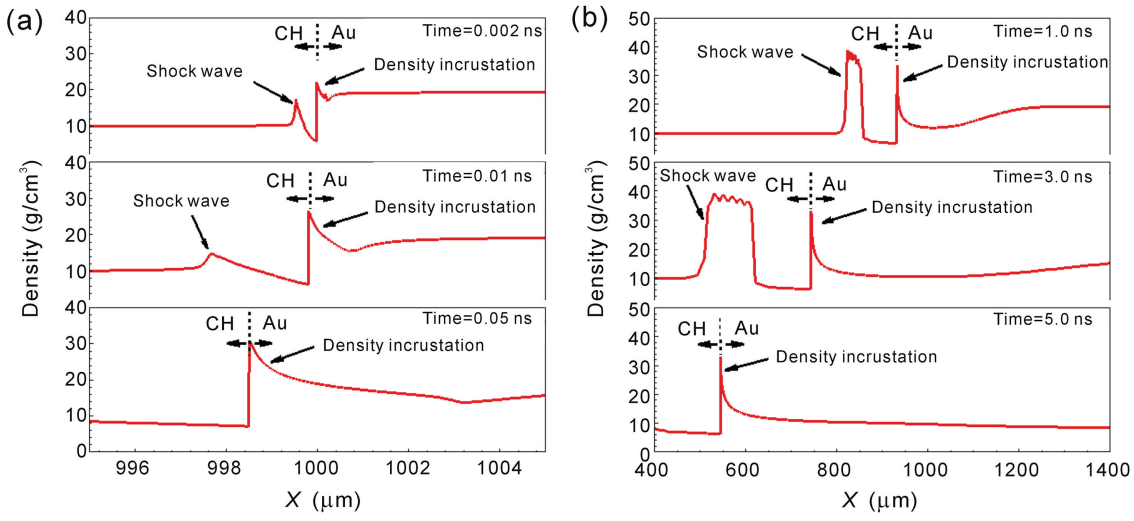

Fig. 2. The density distributions near the CH-Au interface (a) from 0.002 ns to 0.05 ns and (b) from 1.0 ns to 5.0 ns.

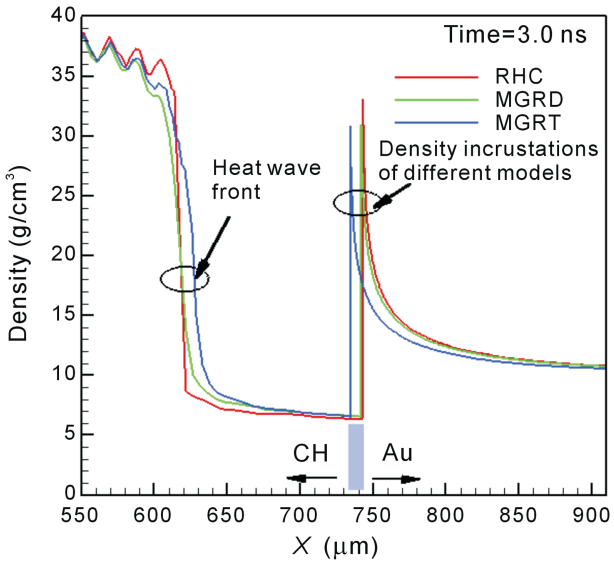

Fig. 3. The density distributions near the Au/CH interface at 3.0 ns. The red line denotes the result of the radiative heat conduction approximation (RHC); the green line denotes the result of the 20-group radiation diffusion approximation (MGRD); the blue line denotes the result of the 20-group radiation transfer equations (MGRT).

the mesh size of the simulation. Taking this into account, the density distributions simulated in both coarse and fine meshes at 3.0 ns are shown in Fig. 4. It can be seen that the height and the profile of the density incrustation are independent of the mesh size, which proves that the density incrustation is not caused by the effect of wall heating. We haven't found other numerical artifacts which might result in the incrustation.

The Rosseland optical depth of the density incrustation is about 50–100, suggesting that the region of density incrustation is optically thick. In the model using coarse meshes, the Rosseland optical depth per mesh near the Au surface is about 0.2, which indicates that the resolution of our meshes is good enough for the radiative transfer calculation.

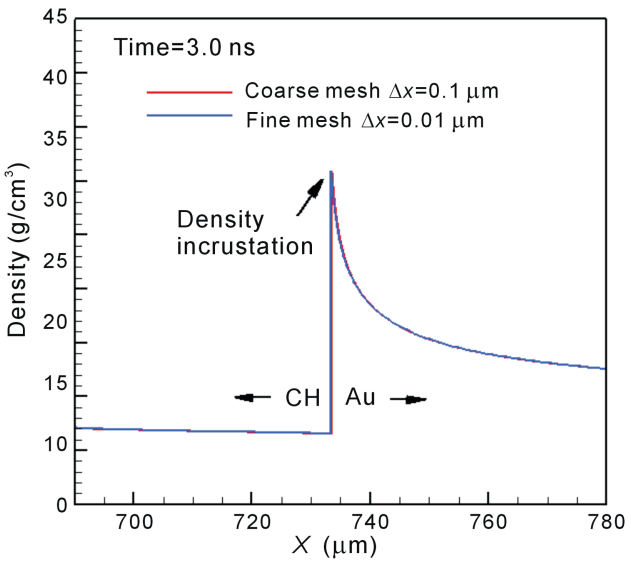

Fig. 4. The density incrustations in coarse meshes and fine meshes.

The density, radiation flux, temperature and pressure distributions near the CH-Au interface are displayed in Fig. 5. It is shown that the temperature decreases rapidly while the pressure remains almost constant in the Au plasmas near the interface. In this process, the radiation pressure in the Au and CH plasmas accounts for less than 1.5 percent of the total pressure, suggesting that it is not important in the evolution of density curst. There are two spatial scales in the Au plasmas. The first is the scale of hydrodynamic motion, which is equal to the maximum local sound speed multiplied by time. For this spatial scale, the pressure of Au plasmas changes due to hydrodynamic motion. The second is the scale of radiation diffusion, which is equal to the mean free path (MFP) of photons in Au plasmas. For the second spatial scale, the temperature of Au plasmas changes due to radiation transport. In this system, the first scale is much larger than the second one.

At the early stage, the high-temperature Au plasmas release energy to the cold CH plasmas due to radiation transport, so that a thin layer of Au plasmas (referred to as the cooling layer) at the interface becomes colder than the inner Au plasmas. The size of the cooling layer is larger compared to the Rosseland MFP of Au plasmas, and is smaller compared to the spatial scale of hydrodynamic motion. Thus the temperature of Au plasmas changes obviously in the cooling layer while the pressure remains nearly constant. In order to maintain the pressure, the density of Au plasmas in the cooling layer is compressed to a higher value. The height of the density incrustation is 30.7 g/cm^3, which is about 1.5 times as much as the initial magnitude. The width of the density incrustation (defined as the full width at 70% of the peak) is 2.6 μm.

Fig. 5 also gives the radiation flux distribution near the CH/Au interface. Since the radiation pressure is small, the radiation energy density can also be neglected compared with the plasma energy density. Thus the slope of radiation flux represents the energy loss/absorption rate of the local plasma to/

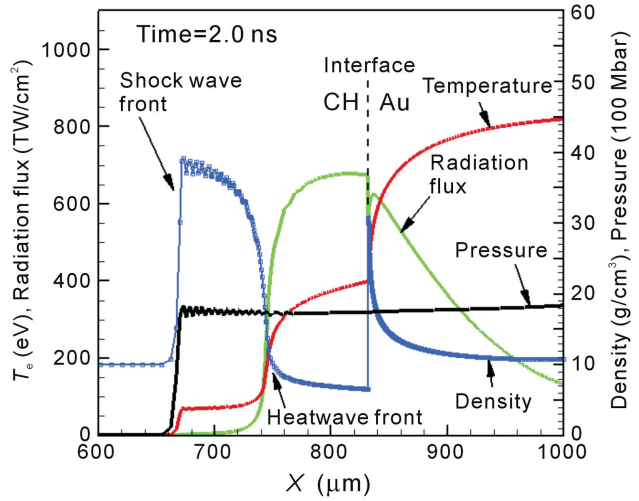

Fig. 5. The temperature, radiation flux, density and pressure distributions near the CH-Au interface at 2.0 ns. The squares in the density distribution curve represent the simulation meshes. The positive value of radiation flux means that the direction of radiation flux is from right to left.

from the radiation field. In the cooling layer and rare zone of the rarefaction wave, the slope is negative, indicating that the plasmas continually release energy to the radiation field. There is a variation of radiation flux in Au plasma near the interface, where the curve seems to be discontinuous. However, when the plot is zoomed in near the interface, it is found that the radiation flux is continuous, and the region of variation is less than the Rosseland mean free path (MFP), suggesting that this phenomenon is caused by the leaking of radiation energy at the boundary.

We developed a simplified analytical model to calculate the profile of the density incrustation. In this model, we made several assumptions: firstly, the radiation transport process in the Au plasma can be described by the radiation heat conduction model; secondly, the pressure is balanced in the cold layer, which means that there is no hydrodynamic motion if the coordinates are set along with the CH/Au interface; thirdly, the cold layer region is in the steady state, which means that the temperature of this region doesn't alter obviously. Based on these assumptions, the radiation transport process in the cold layer is determined by the following equation:

$$\frac{\partial}{\partial x}\left(\kappa\frac{\partial T}{\partial x}\right)=0, \tag{4}$$

where T is the temperature of the plasmas, κ is the heat conduction coefficient, which can be expressed as:

$$\kappa=\frac{16\sigma T^3}{3K\rho}, \tag{5}$$

where σ is the Stefan−Boltzmann constant, K is the opacity of the plasmas. Following Hammer and Rosen's work [31], the opacity and the EOS of Au plasma can be expressed as:

$$\frac{1}{K}=gT^{\alpha}\rho^{\beta}, \tag{6}$$

$$p=rfT^{\mu}\rho^{\nu}. \tag{7}$$

If the temperature range of Au plasma is 1−2 HeV, T is in the unit of HeV, ρ is in g/cm^3, then the constants in Eqs. (6) and (7) are set as:

$$\begin{aligned} &g=\frac{1}{7200}\,\mathrm{g/cm^2},\ \alpha=1.5,\ \beta=-0.2,\ rf=0.85\,\mathrm{MJ/g},\\ &\mu=1.6,\ \nu=0.86. \end{aligned} \tag{8}$$

According to the second assumption, the pressure in the cold layer satisfies:

$$p=rfT^{\mu}\rho^{\nu}=p_{\mathrm{s}}, \tag{9}$$

where p_{s} is the pressure at the CH/Au interface. By substituting Eq. (7) into Eq. (6), $1/K$ can be expressed as:

$$\frac{1}{K}=\frac{g}{(rf)^{\frac{\beta}{\nu}}}T^{\frac{\alpha\nu-\beta\mu}{\nu}}p^{\frac{\beta}{\nu}}. \tag{10}$$

By substituting Eqs. (5), (9) and (10) into Eq. (4), we get the following differential equation:

$$\frac{\partial^2}{\partial x^2}T^{\eta}=0, \tag{11}$$

where

$$\eta=\alpha-\frac{\mu}{\nu}(\beta-1)+4. \tag{12}$$

Integrating Eq. (11) from the CH/Au interface to the interior of Au plasmas, we can find the solution as

$$T=T_{\mathrm{s}}\left[1+\frac{F_{\mathrm{s}}\eta(rf)^{\lambda}}{\frac{16}{3}\sigma g p_{\mathrm{s}}^{\lambda}T_{\mathrm{s}}^{\eta}}x\right]^{\frac{1}{\eta}}, \tag{13}$$

where T_{s}, F_{s} are the temperature and radiation flux at the CH/Au interface, and $\lambda=\beta-1/\nu$. The density distribution can be expressed as

$$\rho=\rho_{\mathrm{s}}\left[1+\frac{F_{\mathrm{s}}\eta(rf)^{\lambda}}{\frac{16}{3}\sigma g p_{\mathrm{s}}^{\lambda}T_{\mathrm{s}}^{\eta}}x\right]^{-\frac{\mu}{\nu\eta}}, \tag{14}$$

where

$$\rho_{\mathrm{s}}=\left(\frac{p_{\mathrm{s}}}{rfT_{\mathrm{s}}^{\mu}}\right)^{\frac{1}{\nu}} \tag{15}$$

is the height (i.e. peak density) of the density incrustation.

We can also give a brief discussion on the width of the incrustation. From Eq. (14), we can define the spatial scale of the incrustation l_{s} as

$$\rho=\rho_{\mathrm{s}}\left[1+\frac{x}{l_{\mathrm{s}}}\right]^{-\frac{\mu}{\nu\eta}}, \tag{16}$$

where

$$l_{\mathrm{s}}=\frac{\frac{16}{3}\sigma g p_{\mathrm{s}}^{\lambda}T_{\mathrm{s}}^{\eta}}{F_{\mathrm{s}}\eta(rf)^{\lambda}}. \tag{17}$$

From Eq. (16), we can find that the width of the incrustation is proportional to l_{s}. Supposing the albedo of the CH plasma at the CH/Au interface is α_{CH}, the boundary flux F_{s} can be expressed as:

$$F_{\mathrm{s}}=(1-\alpha_{\mathrm{CH}})\sigma T_{\mathrm{s}}^4. \tag{18}$$

Substituting Eq. (18) into Eq. (17), we can find that

$$l_{\mathrm{s}}=\frac{\frac{16}{3}g p_{\mathrm{s}}^{\lambda}T_{\mathrm{s}}^{\eta-4}}{(1-\alpha_{\mathrm{CH}})\eta(rf)^{\lambda}}. \tag{19}$$

Eq. (19) shows that in the system with constant boundary pressure p_{s} and constant boundary temperature T_{s}, the width of the incrustation is proportional to the parameter g, which is inversely proportional to the Au opacity K_{Au}.

Fig. 6 gives the comparison between the analytical and simulation profiles of the density incrustation. The analytical curve shows that the density profile of Au plasmas forms a density incrustation near the CH/Au interface. Comparing the analytical curve with simulation results, we find that the width

of the analytical curve is larger than the simulation result. This phenomenon has two possible reasons. The first reason is the assumption that the cold layer is in the steady state. This assumption requires that the radiation flux is constant in the cold layer. However, Fig. 5 shows that the radiation flux varies in the cold layer region, which may lead to the difference between the analytical and simulation results. The second reason is that the constants in Eq. (8) are fitted from the opacity and EOS data in the temperature range of 1–2 HeV. In our simulation, the temperature range of Au plasma is 3–10 HeV. Therefore these constants may not be good fitting results of the opacity and EOS of Au plasmas in our model. The analytical model is only a simple model of the density incrustations, which can give the relative density distribution of the incrustation but cannot give the peak density of the incrustation.

Eq. (14) shows that how the profile of density incrustation is influenced by the boundary flux and the Au opacity. In this model, the dependence of the boundary flux on Au and CH opacities are complicated. How initial states and material properties affect the height and the profile of the density incrustation is studied by simulations. Fig. 7 shows how the density incrustation is affected by the Au and CH opacities. When the opacity of Au plasmas decreases, the height of the density incrustation diminishes, and its width increases. In this situation, the radiation flux in Au plasmas becomes larger. Accordingly, the temperature of the cooling layer near the Au/CH interface increases, while the density decreases. The detailed data of the height and width of the density incrustation for different Au opacities are presented in Table 1. By fitting these data, we can find that the height and width of the density incrustation are proportional to $K_{Au}^{0.10}$ and $K_{Au}^{-0.97}$ respectively. The dependence of the width on the Au opacity given by simulation is consistent with the analytical results in Eq. (19). Meanwhile, the dependence of peak density on the Au opacity is complex and more work need to be done in the future.

When the CH opacity increases, the height of the density incrustation diminishes, while its width increases, as shown in Fig. 7(b). In this situation, the increase of the CH opacity results in the increase of the albedo of CH plasma α_{CH}. Eq. (19) gives that when α_{CH} increases, the width of the incrustation also increases. The height and width of the density incrustation for different CH opacities are presented in Table 2, which shows that the width of the density incrustation depends on the Au opacity more intensely than on the CH opacity, while the height of the density incrustation is not very sensitive to the CH opacity.

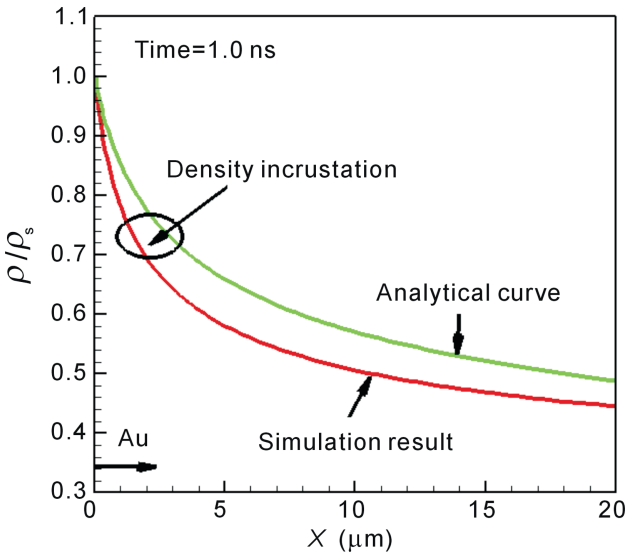

Fig. 6. The comparison of profiles of density incrustation between analytical and simulation results. The horizontal axis is the distance from the CH/Au interface.

Table 1
The height and width of the density incrustation for different Au opacities.

Au opacity factor	Height (g/cm^3)	Width (μm)
2.0	33.2	1.42
1.0	30.7	2.56
0.5	28.5	5.00
0.2	26.3	13.3
0.1	25.3	30.4

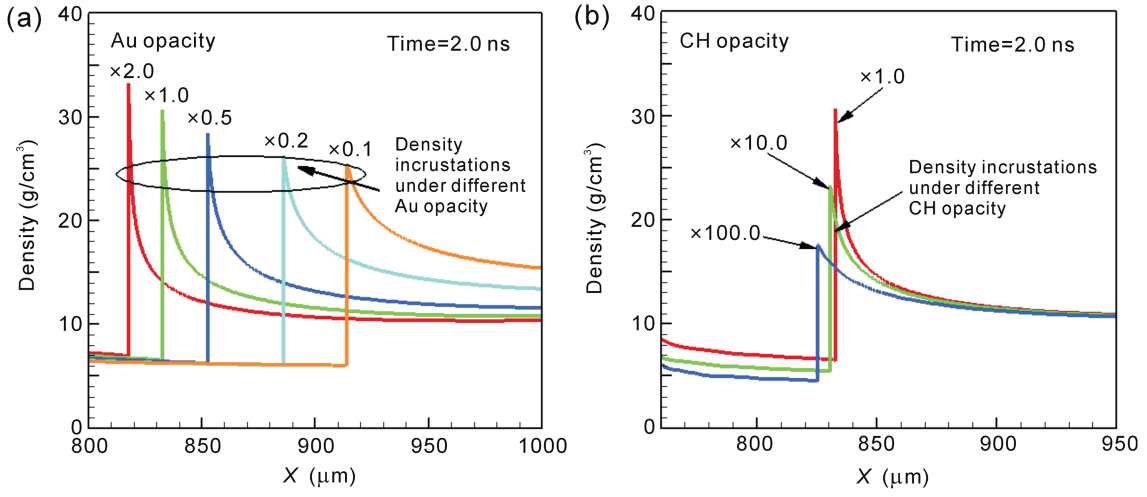

Fig. 7. The density distributions with different (a) Au and (b) CH opacities.

Table 2
The height and width of the density incrustation for different CH opacities.

CH opacity factor	Height (g/cm^3)	Width (μm)
1.0	30.7	2.56
10.0	23.3	8.56
100.0	17.6	38.0

4. Conclusion

According to the above discussions, the density incrustation is a physical phenomenon. Although the density incrustation is displayed only in CH/Au 1-D planar model, this phenomenon is also observed at 1-D spherical geometry with different pairs of materials (CH/Au and D_2/W). Our simulation shows that the density incrustation will appear when three conditions are satisfied: the first is that the high-Z plasmas are in high temperature and continually release energy to low-Z plasmas; the second is that the pressure of low-Z plasmas can confine the expansion of high-Z plasmas; the third is that the difference of the opacity between the high-Z plasmas and the low-Z plasmas is large enough to make the cooling layer thin enough compared with the spatial scale of hydrodynamic motion. This phenomenon can decrease the radiation flux across the high-Z and low-Z material interface.

The phenomenon of density incrustation is important in the implosion processes, in which there is usually RTI near the interface between high-Z and low-Z plasmas. The linear growth rate of RTI is determined by the following equation [32,33].

$$\gamma = \sqrt{\frac{Akg}{1+AkL}}, \tag{20}$$

where A is the Atwood number, k is the wave number, L is the density-gradient scale length, and g is the acceleration. The density incrustations can raise the linear growth rate of the RTI at the interface. In our simulations, the Atwood number of the Au-CH interface increases from 0.31 to 0.59 due to the density incrustation, and the density-gradient scale length diminishes from 54.1 μm to 7.3 μm. When the acceleration of the plasma near the interface is 50 μm/ns^2, the density incrustation makes the linear growth rate of the 10 μm wavelength perturbation rise from 0.91 ns^{-1} to 5.0 ns^{-1}.

Meanwhile, the RTI process mixes the high-Z and low-Z plasmas near the interface, makes the opacity change smoothly. The RTI process makes the opacity of the low-Z plasmas increase and that of the high-Z plasmas decrease near the interface. This process can decrease the height while increase the width of the density incrustation. Thus the density incrustation and the RTI near the interface are coupled with each other. The influence of the density incrustation on the RTI will be investigated in future works. The profile of the density incrustation is related to the radiation transport process in the high-Z plasmas. The experimental investigation on the radiative cooling process is highly expected, and the measurement of the density distribution of high-Z plasma near its interface can be used to verify the material parameters and the radiation hydrodynamic simulations.

Acknowledgements

The authors are grateful to Dr. Yanbo Shi, Dr. Peng Song, Prof. Min Wang, Prof. Jiamin Yang and Prof. Shiyang Zou for their helpful discussions. This work was supported by the National Basic Research Program of China (Grant No. 2013CB922200), the National Natural Science Foundation of China (Grant No. 11025417 and 11405010), and the Science and Technology Developing Foundation of CAEP (Grant no. 2013B0102016).

References

[1] D. Mihalas, B.W. Mihalas, Foundations of Radiation Hydrodynamics, Oxford University Press, 1984.
[2] Y.B. Zel'dovich, Y.P. Raizer, Physics of Shock Waves and High-temperature Hydrodynamic Phenomena, Academic Press, New York, 1967.
[3] R.P. Drake, High Energy Density Physics, Springer-Verlag, New York, 2006.
[4] J. Parrent, B. Friesen, M. Parthasarathy, A review of type Ia supernova spectra, Astrophys. Space Sci. 351 (2014) 1–52.
[5] L. Ensman, A. Burrows, Shock breakout in SN 1987A, Astrophys. J. 393 (1992) 742.
[6] C. Fransson, P. Lundquist, R.A. Chevalier, Circumstellar interaction in SN 1993J, Astrophys. J. 461 (1996) 993–1008.
[7] J.M. Blondin, E.B. Wright, K.J. Borkowski, S.P. Reynolds, Transition to the radiative phase in supernova remnants, Astrophys. J. 500 (1998) 342–354.
[8] J.M. Laming, J. Grun, Dynamical overstability of radiative blast waves: the atomic physics of shock stability, Phys. Rev. Lett. 89 (2002) 125002.
[9] Jacco Vink, Supernova remnants: The X-ray perspective, Astron Astrophys. Rev. 20 (2012) 49.
[10] P.J. Armitage, M. Livio, Hydrodynamics of the stream-disk impact in inter-acting binaries, Astrophys. J. 493 (1998) 898–908.
[11] T.J. Maccarone, Observational tests of the picture of disk accretion, Space Sci. Rev. 183 (2014) 101–120.
[12] R.P. Drake, Theory of radiative shocks in optically thick media, Phys. Plasmas 14 (2007) 043301.
[13] Ryan G. McClarren, R. Paul Drake, J.E. Morel, James Paul Holloway, Theory of radiative shocks in the mixed, optically thick-thin case, Phys. Plasmas 17 (2010) 093301.
[14] J. Bozier, G. Thiell, J. Lebreton, S. Azra, M. Decroisette, et al., Experimental-observation of a radiative wave generated in xenon by a laser-driven supercritical shock, Phys. Rev. Lett. 57 (1986) 1304–1307.
[15] Matthias Gonzalez, Chantal Stehle, Edouard Audit, Michel Busquet, Bedrich Rus, et al., Astrophysical radiative shocks: from modeling to laboratory experiments, Laser Part. Beams 24 (4) (2006) 535–540.
[16] P. Keiter, R. Drake, T. Perry, H. Robey, B. Remington, et al., Observation of a hydrodynamically-driven, radiative-precursor shock, Phys. Rev. Lett. 89 (2002) 165003.
[17] X. Fleury, S. Bouquet, C. Stehle, M. Koenig, D. Batani, et al., A laser experiment for studying radiative shocks in astrophysics, Laser Part. Beams 20 (2002) 263–268.
[18] S. Bouquet, C. Stehle, M. Koenig, J.-P. Chièze, A. Benuzzi-Mounaix, et al., Observation of laser driven supercritical radiative shock precursors, Phys. Rev. Lett. 92 (2004) 225001.
[19] M. Koenig, T. Vinci, A. Benuzzi-Mounaix, N. Ozaki, A. Ravasio, et al., Radiative shocks: An opportunity to study laboratory astrophysics, Phys. Plasmas 13 (2006) 056504.
[20] A.B. Reighard, R.P. Drake, K.K. Dannenberg, D.J. Kremer, M. Grosskopf, et al., Observation of collapsing radiative shocks in laboratory experiments, Phys. Plasmas 13 (2006) 082901.

[21] J. Osterhoff, D.R. Symes, A.D. Edens, A.S. Moore, E. Hellewell, et al., Radiative shell thinning in intense laser-driven blast waves, New J. Phys. 11 (2009) 023022.
[22] A. Diziere, C. Michaut, M. Koenig, C.D. Gregory, A. Ravasio, et al., Highly radiative shock experiments driven by GEKKO XII, Astrophys. Space Sci. 336 (2011) 213−218.
[23] A.J. Visco, R.P. Drake, S.H. Glenzer, T. Döppner, G. Gregori, et al., Measurement of radiative shock properties by X-ray Thomson scattering, Phys. Rev. Lett. 108 (2012) 145001.
[24] G.W. Meng, J.H. Li, J.M. Yang, T. Zhu, S.Y. Zou, et al., A simple method to verify the opacity and equation of state of high-Z plasmas, Phys. Plasmas 20 (2013), 092704.
[25] G. Huser, C. Courtois, M.C. Monteil, Wall and laser spot motion in cylindrical hohlraums, Phys. Plasmas 16 (2009) 032703.
[26] Private communication with Shiyang Zou.
[27] P. Gu, W. Pei, T. Feng, C. Wu, Non-equilibrium radiation emission of the laser illuminated planar target, Sci. China Ser. G 48 (2005) 345.
[28] F.J.D. Serduke, E. Minguez, S.J. Davidson, C.A. Iglesias, WorkOp-IV summary: lessons from iron opacities, JQSRT 65 (2000) 527.
[29] R.E. Peierls, Theory on von Neumann's method of treating shocks, Technical Report LA-332, Los Alamos Scientific Laboratory, 1945.
[30] William J. Rider, Revisiting wall heating, J. Comput. Phys. 162 (2000) 395−410.
[31] J.H. Hammer, M.D. Rosen, A consistent approach to solving the radiation diffusion equation, Phys. Plasmas 10 (5) (2003) 1829.
[32] R. Betti, M. Umansky, V. Lobatchev, V.N. Goncharov, R.L. McCrory, Hot-spot dynamics and deceleration-phase Rayleigh-Taylor instability of imploding inertial confinement fusion capsules, Phys. Plasmas 8 (2001) 5257.
[33] R. Betti, K. Anderson, V.N. Goncharov, R.L. McCrory, D.D. Meyerhofer, et al., Deceleration phase of inertial confinement fusion implosions, Phys. Plasmas 9 (2002) 2277.